catalysts

MDPI

Article

A Combined Computational–Experimental Study on the Substrate Binding and Reaction Mechanism of Salicylic Acid Decarboxylase

Fuqiang Chen [1,2,3,†], Yipei Zhao [1,3,†], Chenghua Zhang [2,3,4], Wei Wang [3,5], Jian Gao [3,5], Qian Li [3,5], Huimin Qin [1], Yujie Dai [1], Weidong Liu [3,5], Fufeng Liu [1,*], Hao Su [3,5,*] and Xiang Sheng [3,5,*]

1 College of Biotechnology, Tianjin University of Science and Technology, Tianjin 300457, China
2 Haihe Laboratory of Synthetic Biology, Tianjin 300308, China
3 Tianjin Institute of Industrial Biotechnology, Chinese Academy of Sciences, Tianjin 300308, China
4 School of Pharmacy, North Sichuan Medical College, Nanchong 637100, China
5 National Center of Technology Innovation for Synthetic Biology and National Engineering Research Center of Industrial Enzymes, Tianjin 300308, China
* Correspondence: fufengliu@tust.edu.cn (F.L.); suhao@tib.cas.cn (H.S.); shengx@tib.cas.cn (X.S.)
† These authors contributed equally to this work.

Abstract: Salicylic acid decarboxylase (SDC) from the amidohydrolase superfamily (AHS) catalyzes the reversible decarboxylation of salicylic acid to form phenol. In this study, the substrate binding mode and reaction mechanism of SDC were investigated using computational and crystallographic methods. Quantum chemical calculations show that the enzyme follows the general mechanism of AHS decarboxylases. Namely, the reaction begins with proton transfer from a metal-coordinated aspartic acid residue (Asp298 in SDC) to the C1 of salicylic acid, which is followed by the C–C bond cleavage, to generate the phenol product and release CO_2. Interestingly, the calculations show that SDC is a Mg-dependent enzyme rather than the previously proposed Zn-dependent, and the substrate is shown to be bidentately coordinated to the metal center in the catalysis, which is also different from the previous proposal. These predictions are corroborated by the crystal structure of SDC solved in complex with the substrate analogue 2-nitrophenol. The mechanistic insights into SDC in the present study provide important information for the rational design of the enzyme.

Keywords: salicylic acid decarboxylase; reaction mechanism; cluster approach; quantum chemical calculations; transition state

Citation: Chen, F.; Zhao, Y.; Zhang, C.; Wang, W.; Gao, J.; Li, Q.; Qin, H.; Dai, Y.; Liu, W.; Liu, F.; et al. A Combined Computational–Experimental Study on the Substrate Binding and Reaction Mechanism of Salicylic Acid Decarboxylase. *Catalysts* **2022**, *12*, 1577. https://doi.org/10.3390/catal12121577

Academic Editors: Jing Zhao and Guochao Xu

Received: 26 October 2022
Accepted: 30 November 2022
Published: 4 December 2022

1. Introduction

Salicylic acid decarboxylase (SDC) catalyzes the reversible decarboxylation of salicylic acid (SA) to form phenol (Scheme 1) [1]. The reaction in the carboxylation direction is a biological alternative to the traditional Kolbe–Schmitt reaction [2]. This method of using enzymes provides a strategy to directly fix CO_2 under mild conditions and the reaction rarely produces by-products, showing high potential for industrial applications [3,4]. The product at the carboxylation direction, salicylic acid, is an important chemical raw material which is commonly used in the production of aspirin drugs [5] and cosmetics [6].

SDC is a metal-dependent decarboxylase belonging to the amidohydrolase superfamily (AHS), which can catalyze the decarboxylation reaction independent of cofactors and O_2. The AHS enzymes share significant structural and mechanistic similarities, especially the unique $(\beta/\alpha)_8$ TIM-barrel fold structure of the active site and divalent metal ions [7]. Interestingly, in previous reports [8–10], the metal ions in the active center of this type of enzyme were often considered as Zn^{2+}. However, in recent studies, it was found that they are Mg^{2+} or Mn^{2+} [11–16].

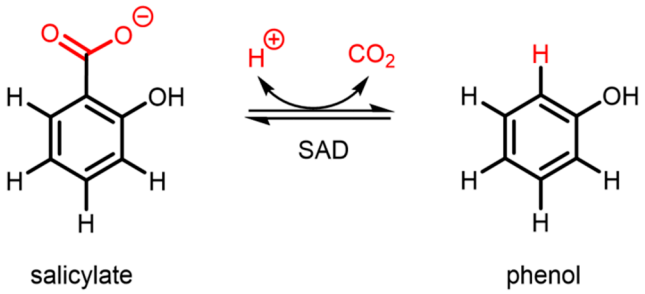

Scheme 1. Reaction catalyzed by salicylic acid decarboxylase (SDC).

Interestingly, SDC is catalytically active toward various aromatic compounds in addition to the natural substrate [17,18], for example, 1-naphthol [19], *p*-aminosalicylic acid [20] and 3-methylsalicylic acid [21]. This further enhances the potential of SDC for industrial applications. Although SDC has a wide substrate spectrum, the wide-type enzyme displays low activity toward non-natural substrates. Thus, protein engineering has been used to produce mutants with improved catalytic performance [20–23].

In a recent study, the crystal structure of SDC from *Trichosporon moniliiforme* in complex with the natural substrate salicylic acid was reported (Figure 1A) [23]. A Zn^{2+} cation was proposed to be the catalytic metal in the active site and to be coordinated by one water, Glu8, His169, Asp298 and SA (Figure 1B). Moreover, molecular dynamics simulations and mutation experiments showed that the mutant MT3 (Y64T/P191G/F195V/E302D) enhanced catalytic activity by expanding the substrate binding pocket. The kinetic parameters K_m and k_{cat} of this enzyme in catalyzing SA decarboxylation were reported as $(1.1 \pm 0.1) \times 10^{-3}$ M and 3.6 ± 0.2 s^{-1}, respectively [23].

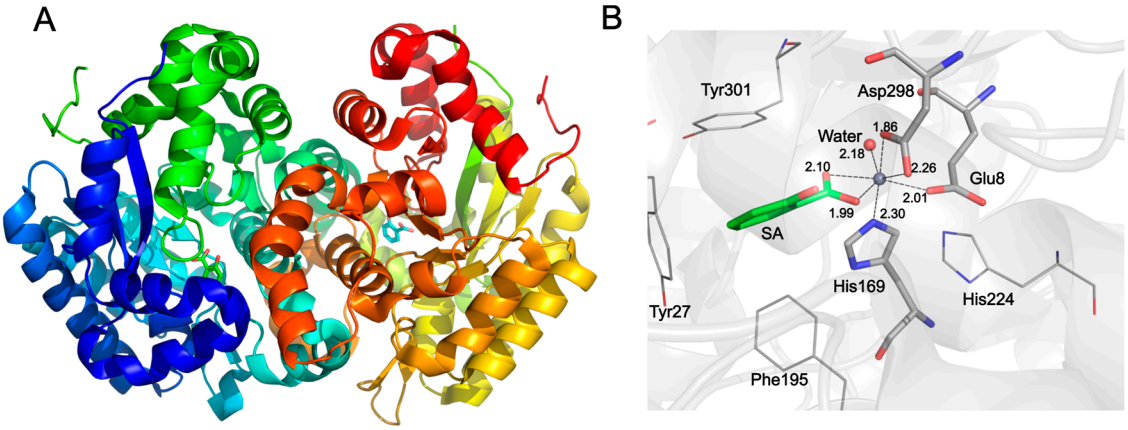

Figure 1. (**A**) Crystal structure and (**B**) active site of salicylic acid decarboxylase (PDB ID: 6JQX).

In the present study, the substrate binding mode and mechanism of the SDC-catalyzed decarboxylation reaction were studied using quantum chemical and experimental approaches. It was shown that SDC adopts a similar substrate binding mode and reaction mechanism to other metal-dependent AHS decarboxylases. Interestingly, our results suggested that the metal of the active center is Mg^{2+}, rather than the previously proposed Zn^{2+}. The detailed information on the substrate binding mode and reaction mechanism obtained in this study could provide useful information to guide the selection of amino acids in the rational design of SDC mutants with improved catalytic efficiency.

2. Results and Discussion

In the previous structural study on SDC [23], the metal ion in the active site was proposed to be Zn^{2+}. However, in our studies on the other decarboxylases from the same family, namely the AHS superfamily, it was found that the metal ion in the active center is

usually Mg^{2+} or Mn^{2+} [11–16]. We thus considered all three types of divalent metals for the entire pathway in the mechanistic study. It turns out that the reaction mechanisms and energy profiles with different metals are very similar; however, the Mg-containing model has the lowest barriers compared to the other two (as discussed below). The enzyme is thus more likely to be Mg-dependent, rather than the previously proposed Zn-dependent [23]. In the following part, we will first discuss the results concerning the Mg-containing system and then the alternatives with Zn^{2+} and Mn^{2+} being the assumed metals in the active site.

In the previously reported crystal structure of SDC in complex with the natural substrate (PDB ID: 6JQX), the substrate was proposed to bind to the metal in a monodentate mode [23]. However, it has been established for the other AHS decarboxylases that the substrate is coordinated to the metal in a bidentate mode and the monodentate mode is in fact unproductive [16]. It is thus interesting to address whether SDC also adopts the bidentate mode in the catalysis. To this end, the structures of the enzyme–substrate complexes with the bidentate mode (called Mode-A) and monodentate mode (called Mode-B) were optimized by using the cluster approach and the corresponding energies were calculated (Figure 2).

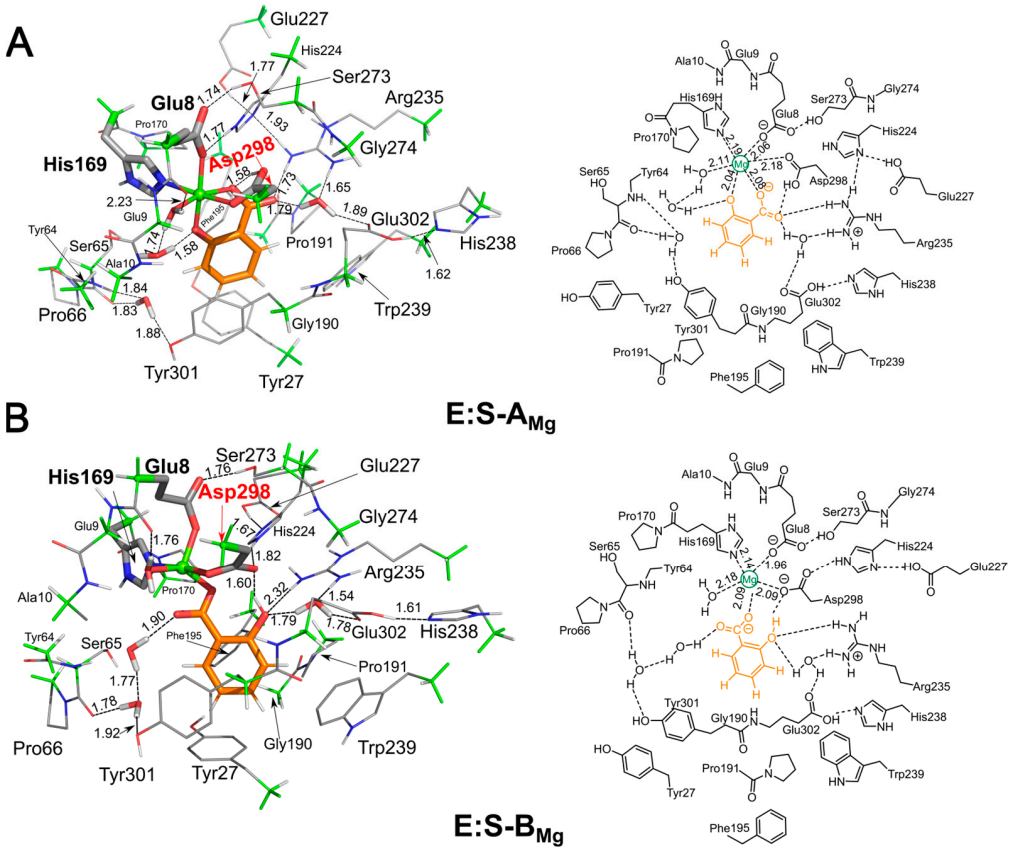

Figure 2. Optimized structures of enzyme–substrate complexes with (**A**) bidentate binding mode and (**B**) monodentate binding mode.

In the optimized structure of Mode-A (**E:S-A$_{Mg}$** in Figure 2A), Asp298 was set to be protonated, while the substrate hydroxyl group was set to be deprotonated due to its coordination to the metal ion. Additionally, an oxygen atom of the substrate carboxylate group was also coordinated to the metal ion. The carboxylate group of the substrate forms hydrogen bonds with a water molecule, Arg235 and Asp298, and the deprotonated hydroxyl group forms a hydrogen bond with another water. In the optimized Mode-B (**E:S-B$_{Mg}$** in Figure 2B), the hydroxyl group of SA is in the neutral form and Asp298 is in the deprotonated state. In addition to the coordination to the metal ion, the carboxylate group

of the substrate also forms a hydrogen bond with the water molecule, which is involved in the hydrogen bond network with another water molecule, Pro66 and Tyr301.

The calculated energies showed that Mode-A is 1.9 kcal/mol lower than Mode-B. In other words, Mode-A is the preferred binding mode in the enzyme–substrate complex. Interestingly, the substrate was previously suggested to bind in a monodentate mode [23]. Since the energy difference between the two modes is not that big, we considered both in the following mechanistic study.

In the pathway with Mode-A (Scheme 2A), the first step of the reaction is the proton transfer from Asp298 to the substrate C1 to form the 2,4-dienone intermediate (**Int-A$_{Mg}$**, Figure 3). The barrier for this step is calculated to be 16.6 kcal/mol, and the energy of the formed intermediate is 9.4 kcal/mol higher than **E:S-A$_{Mg}$** (Figure 4). At the transition state of this step (**TS1-A$_{Mg}$**), the C-H bond distance and the O-H bond distance are 1.35 Å and 1.33 Å, respectively. Subsequently, the C-C bond cleavage takes place to generate the phenol and CO_2 products via the transition state **TS2-A$_{Mg}$**. The energy barrier of this step is 15.8 kcal/mol, and the distance of the breaking C–C bond at **TS2-A$_{Mg}$** is 2.12 Å (Figure 4). The **E:P-A$_{Mg}$** is in energy 0.8 kcal /mol higher than **E:S-A$_{Mg}$**.

According to the calculation results, the energy barrier of the overall reaction is 16.6 kcal/mol, and the rate-limiting step is the proton transfer (Figure 4). The calculated value is in excellent agreement with the experimental data, which is 16.8 kcal/mol converted from the k_{cat} value of 3.6 s^{-1} according to transition state theory [23]. It is interesting to compare the calculate energies of SDC with those of LigW [12], 2,3-DHBD [13], and γ-RSD [15], which also catalyze the decarboxylation of phenolic acids. The barrier of the rate-limiting proton transfer of SDC is found to be similar compared to the corresponding steps of all three other enzymes. For the step of C-C bond cleavage, the energy differences between SDC and the others are larger. However, this does not contribute to the difference in the reaction rate because the proton transfer is the rate-limiting step.

The kinetic isotopic effect (KIE) is helpful in understanding the nature of the rate-limiting step of the catalyzed reaction. We here predict the KIE values for SDC by re-calculating the zero-point energies (ZPEs) of **E:S-A$_{Mg}$** and the rate-limiting **TS1-A$_{Mg}$** by replacing the carboxyl carbon of the substrate with C13 and replacing the proton of Asp298 with deuterium, respectively. The calculated KIE values converted from the energy differences in ZPEs is 5.1 for the proton and 1.0 for the carboxyl carbon.

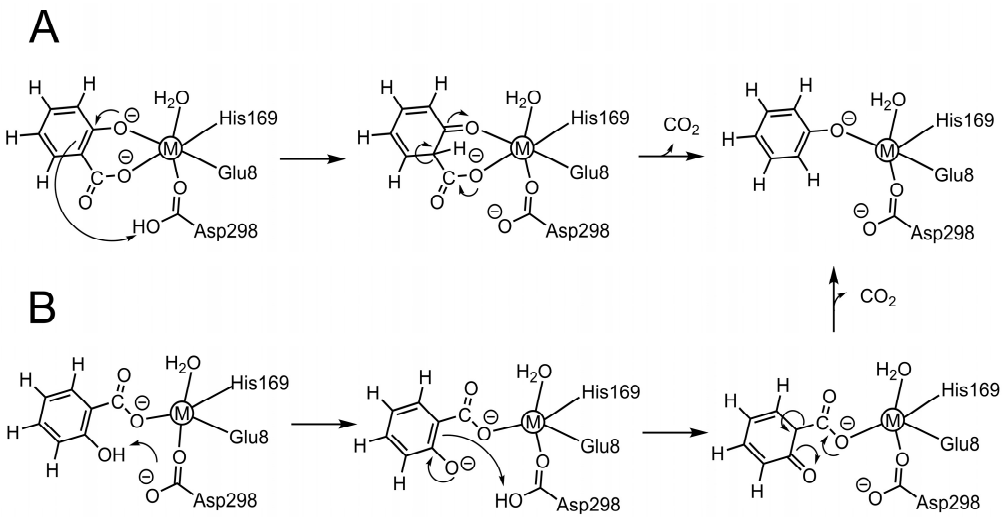

Scheme 2. (**A**) The proposed mechanism of SDC reaction on the basis of calculations in the present study. (**B**) The previously proposed mechanism [19].

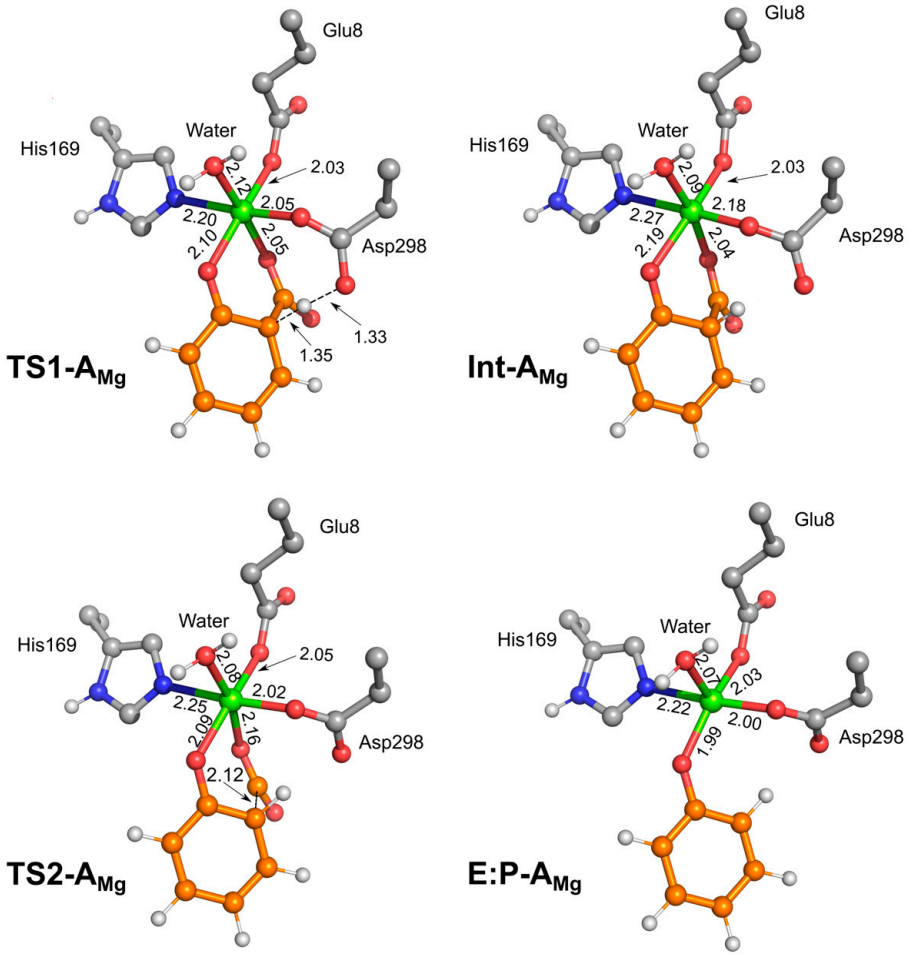

Figure 3. Optimized structures for the transition states (**TS1-A$_{Mg}$** and **TS2-A$_{Mg}$**) and intermediates (**Int-A$_{Mg}$** and **E:P-A$_{Mg}$**) in the reaction pathway of SDC. Only a part of the active site model is shown here. See Supplementary Materials for the structures with full models (Figures S1–S4).

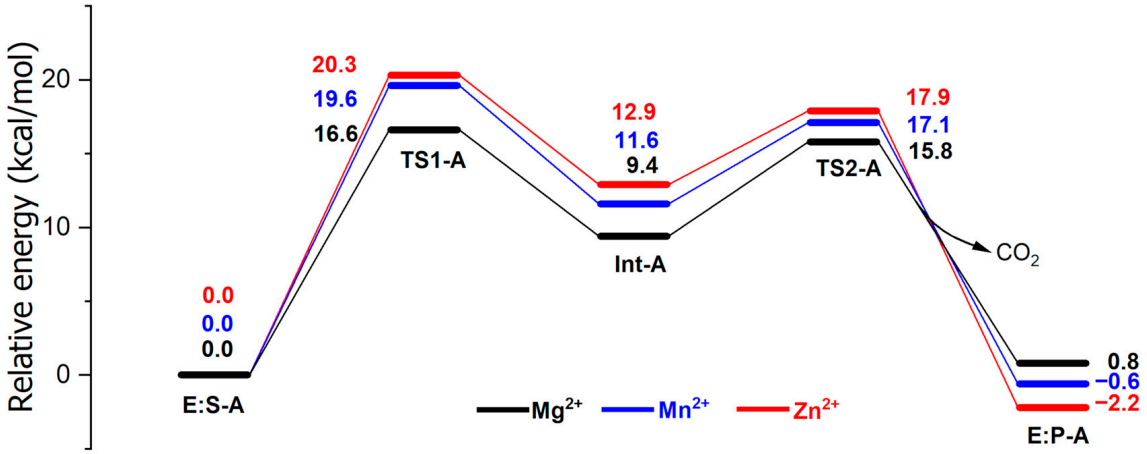

Figure 4. Calculated energy profiles for the decarboxylation reactions catalyzed by SDC with Mg^{2+}, Mn^{2+}, and Zn^{2+}.

In the pathway with Mode-B (Scheme 2B), the reaction first goes through two steps of proton transfer, namely from the hydroxyl group of the substrate to Asp298 and from Asp298 to the substrate C1, which is followed by the C–C bond cleavage to form the products (Scheme 2B). Interestingly, this mechanism was calculated to be energetically

unfavorable with very high barriers. The calculated energy of the transition state for the second proton transfer is 46.5 kcal/mol higher than that of the **E:S-A$_{Mg}$**, and the mechanism with Mode-B is thus obviously infeasible (see Figure S5 for optimized structures).

Since the metal in the active site was previously assumed to be Zn^{2+} [23], we calculated the corresponding energy profiles by using the same active site model as that shown in Figure 2, but the Mg^{2+} was replaced by Zn^{2+} (see Figures S6–S11 for optimized structures). The calculation results show that in the case of Zn-enzyme the energy of Mode-A is very similar to that of Mode-B (only 0.7 kcal/mol in favor of the former). However, the energy barrier of the pathway with Mode-A is 20.3 kcal/mol, which is 3.7 kcal/mol higher than that of the corresponding pathway of Mg-enzyme (Figure 4). Moreover, similar to that of the Mg-enzyme, the barrier of the proton transfer from Asp298 to the substrate C1 in the pathway with Mode-B is also very high (42.4 kcal/mol relative to the corresponding enzyme–substrate complex). Since Mode-B has been shown with significantly high barriers for both Mg- and Zn-containing models, for the examined scenario with the Mn-containing model we considered only the pathway with Mode-A (Figures S12–S17). It turns out that the calculated barrier of the overall reaction is also higher than the Mg-enzyme (by 3.0 kcal/mol, Figure 4).

According to the cluster calculations discussed above, the SDC enzyme is more likely to be Mg-dependent and the substrate is coordinated to the metal in a bidentate mode. To verify these predictions, we solved the crystal structure of SDC in complex with substrate analogue 2-nitrophenol (PDB ID: 8H41, see Table S1 for the data collection and refinement statistics). Analyses on the active site structure provide strong support to the prediction on the basis of the calculations.

First, the previously proposed Zn^{2+} is too negative to fit the electron density map of the metal binding site (Figure 5A). The metal in the active site might be an atom with fewer electrons, such as the computationally predicted Mg^{2+} (Figure 5C). The fitting result with Mg^{2+} indeed shows a perfect match. By using Mn^{2+}, the electron density is slightly overestimated (Figure 5B). Thus, SDC is a Mg-dependent enzyme. Furthermore, the overall structure of SDC obtained in the present study (Figure 5D) is almost identical to the previously solved structure shown in Figure 1A. However, interestingly, the close-view of the active site clearly showed that 2-nitrophenol is coordinated in a bidentate mode (Figure 5E), consistent with the lowest energy and productive binding mode for the natural substrate on the basis of calculations. Another interesting point here is that the measured angle between the nitro group and the phenyl ring is only ca 5°. This is different from the other AHS decarboxylase LigW, for which the substrate analog in the solved X-ray structure was observed to be significantly distorted [11].

Taken together, the calculations predict, from an energetical point of view, that SDC is a Mg-dependent enzyme and show that the reaction follows the general mechanism of AHS decarboxylases consisting of the first proton transfer from a metal-coordinated aspartic acid and the following C-C bond cleavage, in which the substrate is coordinated to the metal in a bidentate mode. Crystallographic study provides support to the metal identity and binding mode of the substrate.

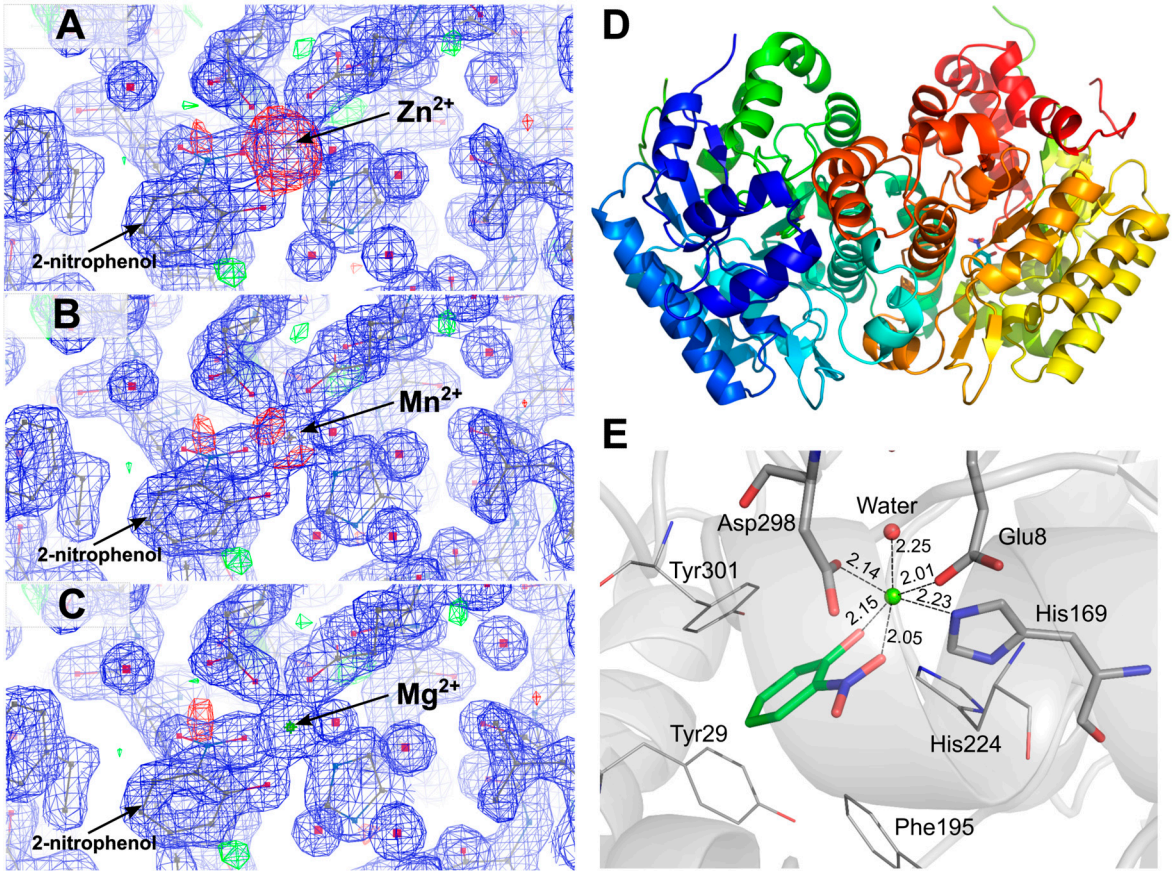

Figure 5. Electron density map ($2F_{obs}$-F_{calc}) of models with (**A**) Zn^{2+}, (**B**) Mn^{2+}, or (**C**) Mg^{2+} in blue, contoured at 1.5 sigma, and the difference map (F_{obs}-F_{calc}) is at 3.0 sigma. The B factors at full occupancy are 44.05 (Chain A) and 43.32 (Chain B) for Zn^{2+}, 36.64 (Chain A) and 36.69 (Chain B) for Mn^{2+}, and 16.79 (Chain A) and 16.97 (Chain B) for Mg^{2+}. The average B factor for all atoms of the structure is 18.53, and the average B factor for all atoms of the ligand is 18.94. (**D**) Overall structure and (**E**) active site structure of SDC in complex with 2-nitrophenol (PDB ID: 8H41).

3. Computational and Experimental Details

3.1. Computational Details

All calculations in this study were performed using the Gaussian 16 program [24], with B3LYP-D3(BJ) hybrid functional [25–28]. In the geometry optimizations, the 6-31G (d,p) basis set was used for the C, H, O, and N atoms, and the LANL2DZ pseudopotential basis set was used for the divalent metal ions [29]. Frequency calculations were performed at the same theoretical level as geometric optimization to obtain the zero-point energies (ZPEs). To consider the effect of protein surrounding which is not included in the active site model, the single-point energy calculations were performed using the SMD model with a dielectric $\varepsilon = 4.0$ at the same level of theory [30]. To obtain more accurate energies, single-point energy calculations were carried out with a larger basis set, namely 6-311+G (2d,2p) for C, H, O, and N atoms and LANL2DZ for divalent metal ions. ZPE and solvation effects were added to the single point energies from the large basis set calculations. According to previous studies on the decarboxylation reactions, the entropy gain generated from CO_2 release was estimated by its translational entropy, which is calculated to be 11.1 kcal/mol at room temperature. This value was added to the energy of the decarboxylation step [12–15,31–34].

3.2. Active Site Model

The quantum chemical cluster approach is employed in the present study. This method has been proven to be very powerful in investigating various aspects of enzymatic

reactions [35–39]. The active site model used for the calculations was designed based on the crystal structure of SDC from *Trichosporon moniliiforme* in complex with the substrate (PDB ID: 6JQX) [23]. The model consists of the metal ion along with its ligands (Glu8, His169, Asp298, a water molecule, and salicylic acid) and other residues making up the active sites (Glu9, Ala10, Tyr27, Tyr64, Ser65, Pro66, Pro170, Gly190, Pro191, Phe195, His224, Glu227, Arg235, His238, Trp239, Ser273, Tyr301, and Glu302). Additionally, three other crystallographic water molecules were also included in the model. The truncations in the model were made at the α-carbons of the amino acid and hydrogen atoms were added to saturate the carbon. To maintain the overall structure of the active site, the truncated carbons and a number of hydrogens were kept fixed during the geometry optimization. The model consists of 322 atoms and has a total charge of 0.

3.3. Cloning and Protein Purification

The *Tm*Sdc gene (GenBank accession number DM040453) was cloned into the pQE80L vector. The pQE80L-TmSdc plasmid was transformed into an *E. coli* BL21(DE3) cell which was grown in LB medium at 37 °C to an OD600 of ~0.8 and then induced by 0.5 mM isopropyl β-D-thiogalactopyranoside (IPTG) at 16 °C for 20 h. Cells were harvested by centrifugation at 5000× *g* for 15 min and then re-suspended in lysis buffer containing 25 mM Tris-HCl, pH 7.5, 150 mM NaCl, and 20 mM imidazole, followed by disruption with a French Press. Cell debris was removed by centrifugation at 17,000× *g* for 1 h. The supernatant was then applied to a Ni-NTA column with an FPLC system (GE Healthcare). The target proteins eluted at ~100 mM imidazole when using a 20–250 mM imidazole gradient. Each protein was dialyzed against a buffer containing 25 mM Tris-HCl, pH 7.5, and loaded onto a Q Sepharose column. Target proteins were eluted at ~200 mM NaCl when using a 0–500 mM NaCl gradient. The purified proteins were passed through a Superdex 200 column and further concentrated to 8 mg/mL in buffer containing 25 mM Tris-HCl (pH 7.5) and 150 mM NaCl. The purity of each protein (>95%) was checked using SDS-PAGE analysis.

3.4. Crystallization, Data Collection, Structure Determination, and Refinement

The optimized crystallization condition of apo-*Tm*Sdc was 24% PEG1000, 0.2 M Tris, pH 7.5. In general, 1 μL protein (8 mg/mL) was mixed with 1 μL of reservoir solution in 24 well Cryschem Plates, and equilibrated against 300 μL of the reservoir. The *Tm*Sdc crystals in complex with 2-nitrophenol were obtained by soaking the apo-*Tm*Sdc crystals in mother liquor containing 10 mM ligand for 1 day. All crystallization experiments were conducted at 25 °C using the sitting-drop vapor-diffusion method. All of the X-ray diffraction data sets were tested and collected at beamlines BL02U1/BL10U2/BL17B/BL18U1/BL19U1 of the National Facility for Protein Science in Shanghai (NFPS) and Shanghai Synchrotron Radiation Facility (SSRF). The diffraction images were processed using HKL2000 [40]. The structure was solved using the molecular replacement (MR) method with Phaser program [41] from the Phenix [42] suite using the structure of TmSdc (PDB ID: 6JQW) [23] as the search model. The further model building and refinement was carried out using programs phenix.refine [43] and Coot [44]. Prior to structural refinements, 5% randomly selected reflections were set aside for calculating R_{free} as a monitor [45]. Data collection and refinement statistics are summarized in Table S1.

4. Conclusions

In the present study, the metal identity, substrate binding mode, and reaction mechanism of salicylic acid decarboxylase (SDC) were investigated using the quantum chemical cluster approach, in combination with crystallographic study. The enzyme is here demonstrated to follow the general mechanism of the amidohydrolase superfamily (AHS). Namely, the reaction starts with the proton transfer from the metal-coordinated aspartic acid (Asp298) to the C1 position of the substrate, which is the rate-limiting step of the entire reaction, and then the C-C bond is broken to form the product. However, very interest-

ingly, and different from the previous proposal, the metal ion in the active site of SDC is found to be Mg^{2+}, and the substrate binds to Mg^{2+} in a bidentate mode. Namely, both the carboxylate group and the phenolic hydroxyl group of the substrate are coordinated to the metal ion. These calculation results are corroborated by the solved crystal structure of SDC in complex with the substrate analogue 2-nitrophenol. The obtained information on the substrate binding mode and the reaction mechanism would be helpful in guiding the selection of targeted sites for mutation in protein engineering.

Supplementary Materials: The following supporting information can be downloaded at: https://www.mdpi.com/article/10.3390/catal12121577/s1, the data collection and refinement statistics of TmSDC crystal, additional calculation results for the Mg-, Mn- and Zn-systems and the Cartesian coordinates of the optimized structures.

Author Contributions: Conceptualization, X.S., H.S. and W.L.; Formal Analysis, F.C., Y.Z., C.Z., W.W., J.G., Q.L., H.Q., Y.D., W.L., F.L., H.S. and X.S.; Investigation, F.C., Y.Z., J.G. and Q.L.; Writing—Original Draft Preparation, F.C., Y.Z. and W.L.; Writing—Review and Editing, X.S. and H.S.; Supervision, W.L., F.L., H.S. and X.S.; Funding Acquisition, X.S., C.Z. and Y.D. All authors have read and agreed to the published version of the manuscript.

Funding: This work was financially supported by the National Key R&D Program of China (2021YFA0911500) and the Tianjin Synthetic Biotechnology Innovation Capacity Improvement Project (TSBICIP-CXRC-026). C.Z. thanks the Bureau of Science and Technology Nanchong City (20SXQT0161) for financial support. Y.D. thanks the Natural Science Foundation of Tianjin (19JCZDJC34800) for the financial support.

Data Availability Statement: Not applicable.

Acknowledgments: We thank the staff from the BL02U1/BL10U2/BL17B/BL18U1/BL19U1 beamlines of the National Facility for Protein Science in Shanghai (NFPS) and Shanghai Synchrotron Radiation Facility (SSRF) for assistance during data collection.

Conflicts of Interest: The authors declare no conflict of interest.

References

1. Kirimura, K.; Gunji, H.; Wakayama, R.; Hattori, T.; Ishii, Y. Enzymatic Kolbe–Schmitt Reaction to Form Salicylic Acid from Phenol: Enzymatic Characterization and Gene Identification of a Novel Enzyme, Trichosporon Moniliiforme Salicylic Acid Decarboxylase. *Biochem. Biophys. Res. Commun.* **2010**, *394*, 279–284. [CrossRef] [PubMed]
2. Lindsey, A.S.; Jeskey, H. The Kolbe-Schmitt Reaction. *Chem. Rev.* **1957**, *57*, 583–620. [CrossRef]
3. Luo, J.; Larrosa, I. C−H Carboxylation of Aromatic Compounds through CO_2 Fixation. *ChemSusChem* **2017**, *10*, 3317–3332. [CrossRef] [PubMed]
4. Plasch, K.; Hofer, G.; Keller, W.; Hay, S.; Heyes, D.J.; Dennig, A.; Glueck, S.M.; Faber, K. Pressurized CO_2 as a Carboxylating Agent for the Biocatalytic Ortho-Carboxylation of Resorcinol. *Green Chem.* **2018**, *20*, 1754–1759. [CrossRef]
5. Boullard, O.; Leblanc, H.; Besson, B. Salicylic Acid. In *Ullmann's Encyclopedia of Industrial Chemistry*; Wiley-VCH Verlag GmbH & Co. KGaA: Weinheim, Germany, 2000; p. a23_477. ISBN 978-3-527-30673-2.
6. Madan, R.K.; Levitt, J. A Review of Toxicity from Topical Salicylic Acid Preparations. *J. Am. Acad. Dermatol.* **2014**, *70*, 788–792. [CrossRef] [PubMed]
7. Seibert, C.M.; Raushel, F.M. Structural and Catalytic Diversity within the Amidohydrolase Superfamily. *Biochemistry* **2005**, *44*, 6383–6391. [CrossRef]
8. Song, M.; Zhang, X.; Liu, W.; Feng, J.; Cui, Y.; Yao, P.; Wang, M.; Guo, R.-T.; Wu, Q.; Zhu, D. 2,3-Dihydroxybenzoic Acid Decarboxylase from Fusarium Oxysporum: Crystal Structures and Substrate Recognition Mechanism. *ChemBioChem* **2020**, *21*, 2950–2956. [CrossRef]
9. Xu, S.; Li, W.; Zhu, J.; Wang, R.; Li, Z.; Xu, G.-L.; Ding, J. Crystal Structures of Isoorotate Decarboxylases Reveal a Novel Catalytic Mechanism of 5-Carboxyl-Uracil Decarboxylation and Shed Light on the Search for DNA Decarboxylase. *Cell Res.* **2013**, *23*, 1296–1309. [CrossRef]
10. Goto, M.; Hayashi, H.; Miyahara, I.; Hirotsu, K.; Yoshida, M.; Oikawa, T. Crystal Structures of Nonoxidative Zinc-Dependent 2,6-Dihydroxybenzoate (γ-Resorcylate) Decarboxylase from Rhizobium Sp. Strain MTP-10005. *J. Biol. Chem.* **2006**, *281*, 34365–34373. [CrossRef]
11. Vladimirova, A.; Patskovsky, Y.; Fedorov, A.A.; Bonanno, J.B.; Fedorov, E.V.; Toro, R.; Hillerich, B.; Seidel, R.D.; Richards, N.G.J.; Almo, S.C.; et al. Substrate Distortion and the Catalytic Reaction Mechanism of 5-Carboxyvanillate Decarboxylase. *J. Am. Chem. Soc.* **2016**, *138*, 826–836. [CrossRef]

12. Sheng, X.; Zhu, W.; Huddleston, J.; Xiang, D.F.; Raushel, F.M.; Richards, N.G.J.; Himo, F. A Combined Experimental-Theoretical Study of the LigW-Catalyzed Decarboxylation of 5-Carboxyvanillate in the Metabolic Pathway for Lignin Degradation. *ACS Catal.* **2017**, *7*, 4968–4974. [CrossRef]
13. Hofer, G.; Sheng, X.; Braeuer, S.; Payer, S.E.; Plasch, K.; Goessler, W.; Faber, K.; Keller, W.; Himo, F.; Glueck, S.M. Metal Ion Promiscuity and Structure of 2,3-Dihydroxybenzoic Acid Decarboxylase of *Aspergillus Oryzae*. *ChemBioChem* **2021**, *22*, 652–656. [CrossRef] [PubMed]
14. Sheng, X.; Plasch, K.; Payer, S.E.; Ertl, C.; Hofer, G.; Keller, W.; Braeuer, S.; Goessler, W.; Glueck, S.M.; Himo, F.; et al. Reaction Mechanism and Substrate Specificity of Iso-Orotate Decarboxylase: A Combined Theoretical and Experimental Study. *Front. Chem.* **2018**, *6*, 608. [CrossRef] [PubMed]
15. Sheng, X.; Patskovsky, Y.; Vladimirova, A.; Bonanno, J.B.; Almo, S.C.; Himo, F.; Raushel, F.M. Mechanism and Structure of γ-Resorcylate Decarboxylase. *Biochemistry* **2018**, *57*, 3167–3175. [CrossRef] [PubMed]
16. Sheng, X.; Himo, F. Mechanisms of Metal-Dependent Non-Redox Decarboxylases from Quantum Chemical Calculations. *Comput. Struct. Biotechnol. J.* **2021**, *19*, 3176–3186. [CrossRef]
17. Wuensch, C.; Glueck, S.M.; Gross, J.; Koszelewski, D.; Schober, M.; Faber, K. Regioselective Enzymatic Carboxylation of Phenols and Hydroxystyrene Derivatives. *Org. Lett.* **2012**, *14*, 1974–1977. [CrossRef]
18. Payer, S.E.; Faber, K.; Glueck, S.M. Non-Oxidative Enzymatic (De)Carboxylation of (Hetero)Aromatics and Acrylic Acid Derivatives. *Adv. Synth. Catal.* **2019**, *361*, 2402–2420. [CrossRef]
19. Ren, P.; Tan, Z.; Zhou, Y.; Tang, H.; Xu, P.; Liu, H.; Zhu, L. Biocatalytic CO_2 Fixation Initiates Selective Oxidative Cracking of 1-Naphthol under Ambient Conditions. *Green Chem.* **2022**, *24*, 4766–4771. [CrossRef]
20. Kirimura, K.; Yanaso, S.; Kosaka, S.; Koyama, K.; Hattori, T.; Ishii, Y. Production of P-Aminosalicylic Acid through Enzymatic Kolbe–Schmitt Reaction Catalyzed by Reversible Salicylic Acid Decarboxylase. *Chem. Lett.* **2011**, *40*, 206–208. [CrossRef]
21. Kirimura, K.; Araki, M.; Ishihara, M.; Ishii, Y. Expanding Substrate Specificity of Salicylate Decarboxylase by Site-Directed Mutagenesis for Expansion of the Entrance Region Connecting to the Substrate Access Tunnel. *Chem. Lett.* **2019**, *48*, 58–61. [CrossRef]
22. Ienaga, S.; Kosaka, S.; Honda, Y.; Ishii, Y.; Kirimura, K. P-Aminosalicylic Acid Production by Enzymatic Kolbe–Schmitt Reaction Using Salicylic Acid Decarboxylases Improved through Site-Directed Mutagenesis. *Bull. Chem. Soc. Jpn.* **2013**, *86*, 628–634. [CrossRef]
23. Gao, X.; Wu, M.; Zhang, W.; Li, C.; Guo, R.-T.; Dai, Y.; Liu, W.; Mao, S.; Lu, F.; Qin, H.-M. Structural Basis of Salicylic Acid Decarboxylase Reveals a Unique Substrate Recognition Mode and Access Channel. *J. Agric. Food Chem.* **2021**, *69*, 11616–11625. [CrossRef] [PubMed]
24. Frisch, M.J.; Trucks, G.W.; Schlegel, H.B.; Scuseria, G.E.; Robb, M.A.; Cheeseman, J.R.; Scalmani, G.; Barone, V.; Petersson, G.A.; Nakatsuji, H.; et al. *Gaussian 16, Revision C.01*; Gaussian, Inc.: Wallingford, CT, USA, 2016.
25. Grimme, S. Density Functional Theory with London Dispersion Corrections. *WIREs Comput. Mol. Sci.* **2011**, *1*, 211–228. [CrossRef]
26. Becke, A.D. Density-functional Thermochemistry. III. The Role of Exact Exchange. *J. Chem. Phys.* **1993**, *98*, 5648–5652. [CrossRef]
27. Lee, C.; Yang, W.; Parr, R.G. Development of the Colle-Salvetti Correlation-Energy Formula into a Functional of the Electron Density. *Phys. Rev. B Condens. Matter* **1988**, *37*, 785–789. [CrossRef]
28. Bursch, M.; Caldeweyher, E.; Hansen, A.; Neugebauer, H.; Ehlert, S.; Grimme, S. Understanding and Quantifying London Dispersion Effects in Organometallic Complexes. *Acc. Chem. Res.* **2019**, *52*, 258–266. [CrossRef]
29. Hay, P.J.; Wadt, W.R. Ab Initio Effective Core Potentials for Molecular Calculations. Potentials for K to Au Including the Outermost Core Orbitals. *J. Chem. Phys.* **1985**, *82*, 299–310. [CrossRef]
30. Marenich, A.V.; Cramer, C.J.; Truhlar, D.G. Universal Solvation Model Based on Solute Electron Density and on a Continuum Model of the Solvent Defined by the Bulk Dielectric Constant and Atomic Surface Tensions. *J. Phys. Chem. B* **2009**, *113*, 6378–6396. [CrossRef]
31. Lind, M.E.S.; Himo, F. Theoretical Study of Reaction Mechanism and Stereoselectivity of Arylmalonate Decarboxylase. *ACS Catal.* **2014**, *4*, 4153–4160. [CrossRef]
32. Sheng, X.; Lind, M.E.S.; Himo, F. Theoretical Study of the Reaction Mechanism of Phenolic Acid Decarboxylase. *FEBS J.* **2015**, *282*, 4703–4713. [CrossRef]
33. Sheng, X.; Himo, F. Mechanism of 3-Methylglutaconyl CoA Decarboxylase AibA/AibB: Pericyclic Reaction versus Direct Decarboxylation. *Angew. Chem. Int. Ed.* **2020**, *59*, 22973–22977. [CrossRef] [PubMed]
34. Planas, F.; Sheng, X.; McLeish, M.J.; Himo, F. A Theoretical Study of the Benzoylformate Decarboxylase Reaction Mechanism. *Front. Chem.* **2018**, *6*, 205. [CrossRef] [PubMed]
35. Himo, F.; de Visser, S.P. Status Report on the Quantum Chemical Cluster Approach for Modeling Enzyme Reactions. *Commun. Chem.* **2022**, *5*, 29. [CrossRef]
36. Siegbahn, P.E.M. A Quantum Chemical Approach for the Mechanisms of Redox-Active Metalloenzymes. *RSC Adv.* **2021**, *11*, 3495–3508. [CrossRef]
37. Himo, F. Recent Trends in Quantum Chemical Modeling of Enzymatic Reactions. *J. Am. Chem. Soc.* **2017**, *139*, 6780–6786. [CrossRef]
38. Blomberg, M.R.A.; Borowski, T.; Himo, F.; Liao, R.-Z.; Siegbahn, P.E.M. Quantum Chemical Studies of Mechanisms for Metalloenzymes. *Chem. Rev.* **2014**, *114*, 3601–3658. [CrossRef]

39. Sheng, X.; Kazemi, M.; Planas, F.; Himo, F. Modeling Enzymatic Enantioselectivity using Quantum Chemical Methodology. *ACS Catal.* **2020**, *10*, 6430–6449. [CrossRef]
40. Otwinowski, Z.; Minor, W. Processing of X-Ray Diffraction Data Collected in Oscillation Mode. *Methods Enzymol.* **1997**, *276*, 307–326. [CrossRef]
41. McCoy, A.J.; Grosse-Kunstleve, R.W.; Adams, P.D.; Winn, M.D.; Storoni, L.C.; Read, R.J. Phaser Crystallographic Software. *J. Appl. Crystallogr.* **2007**, *40*, 658–674. [CrossRef]
42. Adams, P.D.; Afonine, P.V.; Bunkóczi, G.; Chen, V.B.; Davis, I.W.; Echols, N.; Headd, J.J.; Hung, L.-W.; Kapral, G.J.; Grosse-Kunstleve, R.W.; et al. PHENIX: A Comprehensive Python-Based System for Macromolecular Structure Solution. *Acta Crystallogr. D Biol. Crystallogr.* **2010**, *66*, 213–221. [CrossRef]
43. Grosse-Kunstleve, R.W.; Afonine, P.V.; Moriarty, N.W.; Zwart, P.H.; Hung, L.-W.; Read, R.J. Iterative Model Building, Structure Refinement and Density Modification with the PHENIX AutoBuild Wizard. *Acta Crystallogr. D Biol. Crystallogr.* **2008**, *64*, 61–69. [CrossRef]
44. Emsley, P.; Cowtan, K. Coot: Model-Building Tools for Molecular Graphics. *Acta Crystallogr. D Biol. Crystallogr.* **2004**, *60*, 2126–2132. [CrossRef] [PubMed]
45. Brünger, A.T. Assessment of Phase Accuracy by Cross Validation: The Free R Value. Methods and Applications. *Acta Crystallogr. Sect. D* **1993**, *49*, 24–36. [CrossRef] [PubMed]